

MGPATH: Vision-Language Model with Multi-Granular Prompt Learning for Few-Shot WSI Classification

Anh-Tien Nguyen^{1,2,3}
Trung Quoc Nguyen⁸
Miriam Cindy Maurer^{1,2}

Duy Minh Ho Nguyen^{6,7,8*}
Nhat Ho⁵
Daniel Sonntag^{4,8}
Anne-Christin Hauschild^{1,2}

Nghiem Tuong Diep^{8,*}
Jacqueline Michelle Metsch^{1,2}
Hanibal Bohnenberger^{1,2}

¹ University of Göttingen, Germany

² University Medical Center Göttingen, Germany

³ Max Planck Institute for Multidisciplinary Sciences, Germany

⁴ University of Oldenburg, Germany

⁵ The University of Texas at Austin[†], USA

⁶ Max Planck Research School for Intelligent Systems (IMPRS-IS), Germany

⁷ University of Stuttgart, Germany

⁸ German Research Center for Artificial Intelligence (DFKI), Germany

Abstract

Whole slide pathology image classification presents challenges due to gigapixel image sizes and limited annotation labels, hindering model generalization. This paper introduces a prompt learning method to adapt large vision-language models for few-shot pathology classification. We first extend the Prov-GigaPath vision foundation model, pre-trained on 1.3 billion pathology image tiles, into a vision-language model by adding adaptors and aligning it with medical text encoders via contrastive learning on 923K image-text pairs. The model is then used to extract visual features and text embeddings from few-shot annotations and fine-tunes with learnable prompt embeddings. Unlike prior methods that combine prompts with frozen features using prefix embeddings or self-attention, we propose multi-granular attention that compares interactions between learnable prompts with individual image patches and groups of them. This approach improves the model’s ability to capture both fine-grained details and broader context, enhancing its recognition of complex patterns across sub-regions. To further improve accuracy, we leverage (unbalanced) optimal transport-based visual-text distance to secure model robustness by mitigating perturbations that might occur during the data augmentation process. Empirical experiments on lung, kidney, and breast pathology modalities validate the effectiveness of our approach; thereby, we surpass several of the latest competitors and consistently improve performance across diverse architectures, including CLIP, PLIP, and Prov-GigaPath integrated PLIP. We release our implementations and pre-trained models at this [MGPATH](#).

1 Introduction

Whole slide imaging (WSI) [Niazi et al. \[2019\]](#) has become essential in modern pathology for capturing high-resolution digital representations of entire tissue samples, enabling easier digital storage, sharing, and remote analysis [Pantanowitz et al. \[2011\]](#). Unlike conventional methods that depend on examining

* Equal second contribution

slides under a microscope, WSI provides faster, detailed structural and cellular insights essential for disease diagnosis across multiple tissue layers, which is particularly valuable in cancer screening Barker et al. [2016], Cheng et al. [2021]. Nevertheless, WSIs are massive images, often containing billions of pixels Farahani et al. [2015], Song et al. [2023], making detailed annotations and analysis difficult and expensive. To tackle these challenges, machine learning techniques incorporating few-shot and weakly supervised learning have been developed Madabhushi and Lee [2016], Li et al. [2023], Lin et al. [2023], Ryu et al. [2023], Shi et al. [2024]. Among these, *multiple instance learning* (MIL) and *vision-language models* (VLMs) have gained particular attention for their ability to effectively manage limited annotations and interpret complex whole-slide pathology images.

In *MIL* Ilse et al. [2018], Xu et al. [2019a], Li et al. [2023], Lin et al. [2023], Tang et al. [2023], Shi et al. [2023], each WSI is first divided into smaller patches or instances. These instances are extracted feature embeddings using pre-trained vision encoders before being grouped into a "bag", i.e., a whole slide-level representation for the entire WSI. The MIL model mainly focuses on learning ensemble functions to identify patterns in specific patches, contributing to the overall label prediction for each bag (e.g., cancerous or non-cancerous), hence reducing the need for detailed annotations. Nonetheless, these methods often struggle to select relevant patches due to complex correlations and tissue variability Gadermayr and Tschuchnig [2024], Qu et al. [2024b]. To overcome those obstacles, VLMs Lu et al. [2023], Huang et al. [2023], Ikezogwo et al. [2024], Shi et al. [2024] have emerged as a promising solution, combining slide-level visual features with textual descriptions to enrich contextual understanding and support predictions in sparse data scenarios with approaches such as zero-shot learning Xu et al. [2024], Ahmed et al. [2024]. Specifically, VLMs incorporate multi-scale images Shi et al. [2024], Han et al. [2024], permitting the extraction of global and local WSI features at different resolutions. To adapt the pre-trained vision-language model efficiently, prompt learning Zhou et al. [2022b], Gao et al. [2024] is employed where learnable prompts are treated as part of the input text to guide the model, and contextual prompts Li and Liang [2021], Yao et al. [2024] are integrated into feature embeddings using a self-attention mechanism Vaswani [2017]. Despite their strong classification performance across diverse tasks, these approaches still encounter certain limitations.

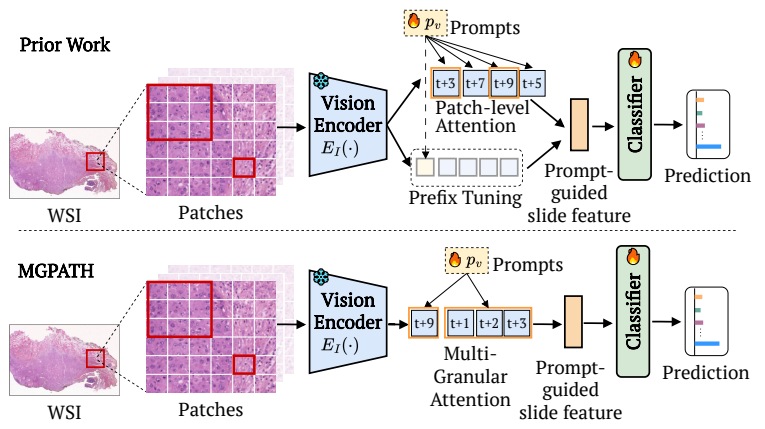


Figure 1: Unlike previous methods that add prompts at prefix positions or patch-level attention - disrupting structural correlations - our MGPATH framework integrates prompts at both regional and individual patch levels (multi-granular attention).

variability Gadermayr and Tschuchnig [2024], Qu et al. [2024b]. To overcome those obstacles, VLMs Lu et al. [2023], Huang et al. [2023], Ikezogwo et al. [2024], Shi et al. [2024] have emerged as a promising solution, combining slide-level visual features with textual descriptions to enrich contextual understanding and support predictions in sparse data scenarios with approaches such as zero-shot learning Xu et al. [2024], Ahmed et al. [2024]. Specifically, VLMs incorporate multi-scale images Shi et al. [2024], Han et al. [2024], permitting the extraction of global and local WSI features at different resolutions. To adapt the pre-trained vision-language model efficiently, prompt learning Zhou et al. [2022b], Gao et al. [2024] is employed where learnable prompts are treated as part of the input text to guide the model, and contextual prompts Li and Liang [2021], Yao et al. [2024] are integrated into feature embeddings using a self-attention mechanism Vaswani [2017]. Despite their strong classification performance across diverse tasks, these approaches still encounter certain limitations.

First, (i) adapting prompt learning with frozen visual features often neglects the hierarchical relationships among learnable prompts and the visual features they interact with - specifically, *the multi-granular attention between prompts to individual patches and groups of patches*. This limitation lessens the model's ability to capture interdependence across distinct scales — from fine-grained local features to broader contextual information, leading to less accurate comprehension of complex

patterns in pathology images. *Second*, (ii) many VLMs rely on the CLIP architecture Radford et al. [2021], which was not explicitly pre-trained on pathology images, thereby limiting its adaptability in few-shot settings, especially when the architecture is primarily frozen and prompt learning is applied. While there exist recent works that have incorporated PLIP Huang et al. [2023], a model pre-trained on 200k pathology image-text pairs curated from Twitter and showed significant improvements, an open question remains whether scaling pre-training to millions or billions of pathology-specific samples could further boost performance. *Lastly*, (iii) most VLM models for whole-slide pathology rely on cosine similarity to align visual and textual features. This metric, however, can struggle with multiple text descriptions for sub-regions Chen et al. [2023] and with augmented data perturbations Nguyen et al. [2024b], as it lacks the precision to capture fine-grained alignments between varied image-text pairs.

In this work, we present **MGPATH**, a novel VLM method developed to address the challenges in whole-slide pathology classification. Our approach begins by adapting **Prov-GigaPath** Xu et al. [2024] - one of the largest pre-trained vision models trained on 1.3 billion pathology image patches - into a vision-language model. We accomplish this through contrastive learning with a pre-trained text encoder from the PLIP model Huang et al. [2023], which was trained on approximately 200K pathology image-text pairs. To strengthen this alignment, we collected an additional 923K image-text pairs from ARCH Gamper and Rajpoot [2021], PatchGastricADC22 Tsuneki and Kanavati [2022] and Quilt-1M Ikezogwo et al. [2024] and trained adaptor-based cross-alignment Gao et al. [2024], Cao et al. [2024] between **Prov-GigaPath**'s visual encoder and PLIP's text encoder. Crucially, only lightweight adaptors are updated, making this process highly parameter-efficient. To the best of our knowledge, **MGPATH** is the first parameter-efficient vision-language model trained for pathology at this data scale — utilizing 923K image-text pairs compared to the 200K in PLIP, and further benefiting from **Prov-GigaPath**'s 1.3 billion sample pre-training.

Next, we leverage these pre-trained models for few-shot WSI tasks by introducing *multi-granular prompt learning*. First, visual embeddings and descriptive text prompts are generated for image patches at different resolutions using large language models, which have been shown to improve performance Han et al. [2024], Shi et al. [2024], Qu et al. [2024a]. Unlike prior methods that concatenate or use basic attention on individual patches Li and Liang [2021], Zhou et al. [2022b], Yao et al. [2024], Shi et al. [2024], our attention integrates learnable prompts with frozen visual features at both fine- and coarse-grained perspectives (Figure 1). We represent image patches from each WSI as a spatial graph, using bounding box coordinates to enable region-level aggregation through message passing along local connections. This spatial structure is encoded as tokens within the *Key-Value* matrices, which interact with *Query* matrices derived from prompt embeddings. By directing attention from *Query* to *Key-Value* matrices across both patch and region levels, our approach effectively captures hierarchical information, enriching feature representation and selectively emphasizing features across diverse tissue areas.

Finally, to measure the distance between prompt-fused visual embedding and multiple text prompts, we resort to the optimal transport (OT) method Nguyen et al. [2021], Pham et al. [2020], Séjourné et al. [2023], Chen et al. [2023], Dong et al. [2023], Nguyen et al. [2024b], Zhan et al. [2021], providing flexibility in aligning heterogeneous data distributions. This property is beneficial in few-shot WSI classification when it can (i) handle data augmentation with noise, as OT can adapt to perturbations without losing meaningful structural relationships, and (ii) capture imbalances masses between two modality embeddings when text prompts only describe sub-regions in WSI samples. Through

extensive evaluations of three datasets with various architectures (CLIP-ResNet50, CLIP-ViT16, PLIP, and (Prov-GigaPath)-integrated PLIP), we observe that **MGPATH** demonstrate consistent improvements over several state-of-the-art MIL and VLM in literature (14 competitors). As an example, **MGPATH** with (Prov-GigaPath)-PLIP variant outperforms **MSCPT** [Han et al. \[2024\]](#) by 5% in F1 and 8% in AUC on the TCGA-BRCA dataset. Additionally, it also surpasses two state-of-the-art VLMs models, **CONCH** [Lu et al. \[2024\]](#) and **QUILT** [Ikezogwo et al. \[2024\]](#), by approximately 6% in accuracy on TCGA-BRCA.

2 Related Work

2.1 Large-scale Pre-trained Models for Pathology

Recent advancements in large-scale pre-trained models for pathology can be broadly classified into two categories. *Vision models*, such as **Virchow** [Ikezogwo et al. \[2024\]](#), **Hibou** [Nechaev et al. \[2024\]](#), **UNI** [Chen et al. \[2024\]](#), and **Prov-GigaPath** [Xu et al. \[2024\]](#) leverage massive pathology image datasets to learn robust visual representations. Among these, **Prov-GigaPath** stands out as the largest model, trained on 1.3 billion pathology image patches, and excels in resolving complex tissue patterns at high resolution. On the other hand, *vision-language models* (VLMs) like **PLIP** [Huang et al. \[2023\]](#) (trained 200K image-text pairs), **CONCH** [Lu et al. \[2024\]](#) (1.17M), or **QUILTNET** [Ikezogwo et al. \[2024\]](#) (1M), integrate visual and textual information to enhance contextual understanding and improve pathology slide interpretation. In contrast, our **MGPATH** combines the strengths of both approaches by using a *parameter-efficient adaptor* to link **Prov-GigaPath** (the largest pre-trained vision encoder) with a text encoder from VLMs like **PLIP** or **CONCH**, leveraging both rich visual features and semantic textual embeddings. Although we use the **PLIP** text encoder in our experiments due to its common use in baselines, the method can be extended to other larger pre-trained text models.

2.2 Few-shot learning in WSI

MIL treats a WSI as a bag of patches and aggregates these instances into a bag of features, with early methods using non-parametric techniques like mean or max pooling. However, since disease-related patches are rare, these methods can overwhelm useful information with irrelevant data. To address this, attention-based methods, graph neural Networks (GNNs), and Transformer-based methods have been introduced [Lu et al. \[2021\]](#), [Chen et al. \[2021\]](#), [Ilse et al. \[2018\]](#), [Li et al. \[2021\]](#), [Shao et al. \[2021\]](#), [Zheng et al. \[2022\]](#). In contrast, VLMs have gained popularity through contrastive learning, aligning image-text pairs to enhance performance on a variety of tasks. While collecting large-scale pathology image-text pairs remains challenging, models like **MI-Zero**, **PLIP**, and **CONCH** have been trained on hundreds of thousands to over a million pathology image-text pairs [Lu et al. \[2023\]](#), [Huang et al. \[2023\]](#), [Lu et al. \[2024\]](#). Some approaches also integrate multi-magnification images and multi-scale text to mimic pathologists’ diagnostic processes, especially for detecting subtle abnormalities [Shi et al. \[2024\]](#), [Han et al. \[2024\]](#). Our **MGPATH** extends on the VLMs strategy by further *amplifying the benefits of using a large pre-trained pathology VLM model* and introducing a new *parameter-efficient multi-granular prompt learning* to adapt these models to few-shot settings.

2.3 Prompt Learning for Vision-Language Adaptations

Prompt tuning is proposed to transfer large pre-trained model task-specific downstream tasks and has shown strong results in multimodal models like CLIP. Rather than design a heuristic template, several methods like **CoOp** Zhou et al. [2022b], **CoCoOp** Zhou et al. [2022a], or **MaPLe** Khattak et al. [2023] among others Rao et al. [2022], Shu et al. [2022] have allowed models to determine optimal prompts from multiple perspectives, such as domain generalization Ge et al. [2023], Yao et al. [2024], knowledge prototype Zhang et al. [2022b], Li et al. [2024], or diversity Lu et al. [2022], Shu et al. [2022]. However, these approaches focus on natural images and do not address the unique challenges of whole-slide pathology images, which require multi-scale and structural contextual information. While a few current methods typically integrate prompts with frozen visual features via self-attention Shi et al. [2024], Qu et al. [2024a], these approaches might struggle with the complex relationships in WSIs. Our solution introduces multi-granular prompt learning, bridging *attention* on both *individual image patches* and *spatial groups* to better align with the hierarchical structure of WSI data.

3 Methods

Figure 2 provides an overview of the key steps in our method. Before diving into the details of each section, we first introduce our PLIP model enhanced by **Prov-GigaPath** through the use of adaptors.

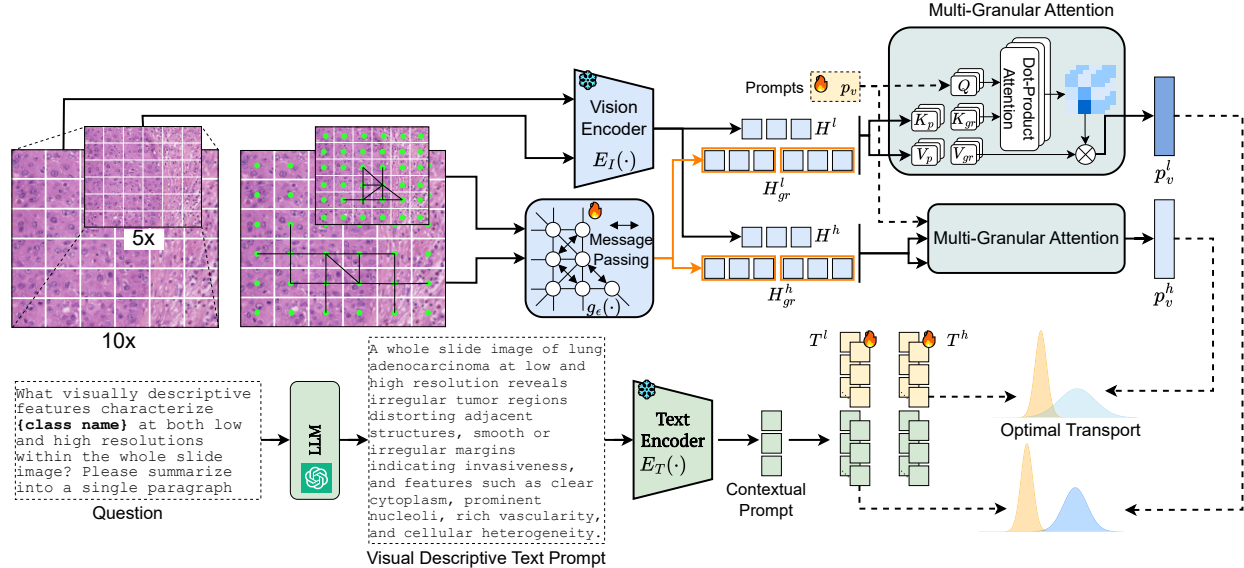


Figure 2: The pipeline of the proposed MGPATH method. Low- and high-resolution image patches are processed with large language models to generate visual contextual descriptions (Section 3.2). Visual prompts are integrated with frozen features through multi-granular attention at both patch and group-of-patch levels 3.3. The final output is obtained by aligning visual and text embeddings using optimal transport (Section 3.4).

3.1 Bridging Pathology Visual and Text Encoders

To leverage **Prov-GigaPath**’s extensive pre-trained visual features for pathology, we implement lightweight adaptors that map image patch-level features to an embedding space aligned with the PLIP text encoder. These adaptors allow us to train joint image-text representations with parameter efficiency by updating only the adaptor weights.

Given a set of collected pathology image-text pairs $\{(\mathbf{I}_i, \mathbf{T}_i) | i = 1, 2.., N\}$ (Sec. 4), we denote by $E_I(\cdot)$ be a pre-trained vision encoder from **Prov-GigaPath**, extracting patch-level feature, and $E_T(\cdot)$ the pre-trained text encoder from PLIP model. Given a batch size of B samples, the image and text embeddings are computed as $\mathbf{x}_i = E_I(\mathbf{I}_i) \in \mathbb{R}^{d_v}$, $\mathbf{t}_i = E_T(\mathbf{T}_i) \in \mathbb{R}^{d_t}$. We then design two trainable adaptors $A_I(\cdot)$ and $A_T(\cdot)$, that maps $(\mathbf{x}_i, \mathbf{t}_i)$ into the same hidden dimension \mathbb{R}^d and minimizes the noise contrastive loss [Oord et al. \[2018\]](#):

$$\mathcal{L}_{con} = \mathbb{E}_B \left[-\log \frac{\exp(\cos(A_I(\mathbf{x}_i), A_T(\mathbf{t}_i))/\tau)}{\sum_j \exp(\cos(A_I(\mathbf{x}_i), A_T(\mathbf{t}_j))/\tau)} \right], \quad (1)$$

where $\cos(\cdot)$ is the cosine similarity, and τ denotes for temperature of the softmax function. For parameter efficiency, we train only the adaptors $A_I(\cdot), A_T(\cdot)$ while keeping the **Prov-GigaPath** visual encoder and PLIP text encoder frozen. After optimizing Eq.(1), we use the outputs of the adaptors as visual and text embeddings for downstream tasks. Unless otherwise specified, we refer to this model as **GigaPath-PLIP**.

3.2 Multi-Magnification Descriptive Text Prompts

To improve vision-language models (VLMs) for whole-slide image (WSI) analysis, designing effective text prompts is essential. Pathologists typically examine WSIs by first assessing tissue structures at low magnification before zooming in to analyze finer details such as nuclear size and shape. Inspired by this diagnostic workflow and the inherently multi-scale nature of WSIs, recent studies [Shi et al. \[2024\]](#), [Han et al. \[2024\]](#) have introduced dual-scale visual descriptive text prompts to guide VLMs, leading to significant improvements in classification performance. Building on this observation, we further extend and refine this strategy to enhance model effectiveness.

First, to ensure that generated prompts remain robust across varying WSI magnifications, we design shared prompts that combine both high- and low-scale descriptive elements, treating them as contextual embeddings. Specifically, we leverage the API of a frozen language model (GPT-4) and query it with the prompt as Figure 3

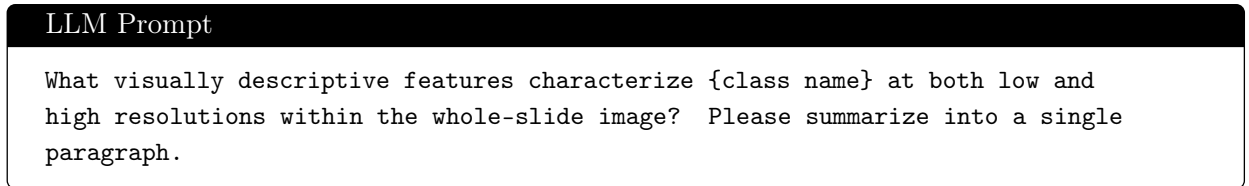


Figure 3: LLM template prompt.

In the above query, we replace `{class name}` by specific categories, for e.g., they are invasive ductal carcinoma (IDC) and invasive lobular carcinoma (ILC) in the TCGA-BRCA dataset.

Second, at each low/high scale, rather than inserting *a single learnable text prompt* of length K alongside a frozen contextual prompt from LLMs [Shi et al. \[2024\]](#), [Han et al. \[2024\]](#), we propose *using M learnable prompts*. This approach aims to capture different sub-regions or structural features within each patch that might be overlooked with only a single prompt. Specifically, we define visual descriptive text prompts for both low and high resolutions as follows:

$$\begin{aligned}\mathbf{T}_i^{(l)} &= \left\{ \left([\omega_i^{(l)}]_1 [\omega_i^{(l)}]_2 \dots [\omega_i^{(l)}]_K [\text{LLM context}] \right) \mid_{i=1}^M \right\} \\ \mathbf{T}_i^{(h)} &= \left\{ \left([\omega_i^{(h)}]_{(1)} [\omega_i^{(h)}]_2 \dots [\omega_i^{(h)}]_K [\text{LLM context}] \right) \mid_{i=1}^M \right\},\end{aligned}\quad (2)$$

where $[\omega_i^\beta]_j, j \in [1, \dots, K], i \in [1, \dots, M]$ are KM *trainable textual prompts* for each resolution $\beta \in \{l, h\}$.

3.3 Granularity-aware Visual Prompt Learning

We propose to adapt visual prompts to frozen features extracted by a pre-trained vision encoder in the VLM model by taking into account the image patch level and spatial groupings of patches. Specifically, for each WSI W , we denote by $\{W^{(l)}, W^{(h)}\}$ are representations of W at low and high magnification. We define a bag of multiple instances of W as $I = \{I^{(l)}, I^{(h)}\}$ where $I^{(l)} \in \mathbb{R}^{N_l \times N_b \times N_b \times 3}$, $I^{(h)} \in \mathbb{R}^{N_h \times N_b \times N_b \times 3}$ with N_l, N_h indicate the number of low and high-resolution image patches and N_b is the patch size. Following prior works [Shi et al. \[2024\]](#), [Ilse et al. \[2018\]](#), [Lu et al. \[2021\]](#), [Han et al. \[2024\]](#), we employ a non-overlapping sliding window technique to extract patches I from the WSI.

3.3.1 Patches-based Prompting

The frozen image encoder $E_I(\cdot)$ (or $A_I(E_I(\cdot))$ in case of **GigaPath-PLIP**) is used to map patches I into a feature vector $H = \{H^{(l)} \in \mathbb{R}^{N_l \times d}, H^{(h)} \in \mathbb{R}^{N_h \times d}\}$ where d denotes the feature dimension. To effectively consolidate the extensive set of patch features into a final slide-level representation, we introduce a set of learnable visual prompts $\mathbf{p}_v \in \mathbb{R}^{N_p \times d}$, which facilitate the progressive merging of patch features in $H^{(l)}$ (similarly for $H^{(h)}$) (Figure 2). In particular, we formulate \mathbf{p}_v as Query and take all features in $H^{(l)}$ as the Keys $K_p^{(l)}$ and Values $V_p^{(l)}$ in in self-attention [Vaswani \[2017\]](#). We then associate \mathbf{p}_v with patch features as:

$$\mathbf{p}_{v,p}^{(l)} = \text{Normalize} \left(\text{SoftMax} \left(\frac{\mathbf{p}_v K_p^{(l)T}}{\sqrt{d}} \right) V_p^{(l)} \right) + \mathbf{p}_v, \quad (3)$$

where $\text{Normalize}(\cdot)$ and $\text{Softmax}(\cdot)$ indicate the layer normalization operator and activation function respectively. Intuitively, Eq.(3) computes the correlations between the visual prompt \mathbf{p}_v and all individual feature patches in $H^{(l)}$, subsequently grouping patches with high similarity to form fused prompt embeddings. However, since cancerous tissues in WSIs often appear as large, contiguous regions of adjacent image patches, this motivates the introduction of spatial patch group-based attention.

3.3.2 Spatial Patch Group-based Prompting

We build spatial correlations for multiple instances in I by using their image patch coordinates inside each WSI W . In particular, taken $I^{(l)} = \{I_1^{(l)}, I_2^{(l)}, \dots, I_{N_l}^{(l)}\}$ with their corresponding extracted

features in $H^{(l)} = \{H_1^{(l)}, H_2^{(l)}, \dots, H_{N_l}^{(l)}\}$, we construct a graph $G^{(l)} = (V^{(l)}, E^{(l)})$ to capture regional tissue structures where the set of vertices $V^{(l)} = I^{(l)}$, and $E^{(l)} \in \{0, 1\}^{N_l \times N_l}$ is the set of edges. Edges in $E^{(l)}$ can be defined by linking inner patches to their K-nearest neighbors based on the coordinates. We define the node-feature embedding as $X^{(l)} = H^{(l)} \in \mathbb{R}^{N_l \times d}$ that associates each vertex $v_i^{(l)}$ with its feature node $x_i^{(l)} = H_i^{(l)}$.

We next design a trainable message-passing network $g_\epsilon(\cdot)$ based on the graph attention layer (GAT) [Veličković et al. \[2017\]](#) to capture the feature representation of each node and its local neighbors. The message passing of the GAT layer is formulated as:

$$\begin{aligned} \alpha_{i,j} &= \frac{\exp\left(\sigma(a_s^T \Theta_s x_i^{(l)} + a_t^T \Theta_t x_j^{(l)})\right)}{\sum_{k \in \mathcal{N}(i) \cup \{i\}} \exp(\sigma(a_s^T \Theta_s x_i^{(l)} + a_t^T \Theta_t x_k^{(l)}))} \\ x_i^{(l)'} &= \alpha_{i,i} \Theta_s x_i^{(l)} + \sum_{j \in \mathcal{N}(i)} \alpha_{i,j} \Theta_t x_j^{(l)}, \end{aligned} \quad (4)$$

where $x_i^{(l)'}$ is aggregated features of $x_i^{(l)}$ with its local region after GAT layer, $\sigma(\cdot)$ is the LeakyReLU activation function, $\mathcal{N}(i)$ denote the neighboring nodes of the i -th node, $\alpha_{i,j}$ are the attention coefficients and $a_s, a_t, \Theta_s, \Theta_t$ are weight parameters of $g_\epsilon(\cdot)$.

After doing a message passing by $g_\epsilon(\cdot)$, the graph of patch-image features $G^{(l)}$ is updated to $G^{(l)'}$, where each node now represents a super-node that encapsulates its corresponding feature region. We then squeeze all feature nodes in $G^{(l)'}$ as a vector $H_{gr}^{(l)}$ and treat them as another Keys $K_{gr}^{(l)}$ and Values $V_{gr}^{(l)}$ for region-level features. Similar to Eq.(3), we associate prompt \mathbf{p}_v with those group-level features:

$$\mathbf{p}_{v,gr}^l = \text{Normalize} \left(\text{SoftMax} \left(\frac{\mathbf{p}_v K_{gr}^{(l)T}}{\sqrt{d}} \right) V_{gr}^{(l)} \right) + \mathbf{p}_v. \quad (5)$$

The final output of our multi-granular is computed as:

$$\mathbf{p}_v^{(l)} = (1 - \alpha) \cdot \mathbf{p}_{v,p}^{(l)} + \alpha \cdot \mathbf{p}_{v,gr}^{(l)}, \quad (6)$$

which interpolates between image patches and spatial patch groups.

3.4 Optimal Transport for Visual-Text Alignment

Given descriptive text prompts $\mathbf{T}^{(l)}$ and $\mathbf{T}^{(h)}$ (Eq.(2)) and visual prompt-guided slide features $\mathbf{p}_v^{(l)}$ and $\mathbf{p}_v^{(h)}$ (Eq.(6)) for low and high resolutions, our goal is to maximize the similarity between slide and text embeddings for each class c . Rather than relying on cosine distance, as in prior works [Zhou et al. \[2022b,a\]](#), [Zhao et al. \[2024\]](#), [Qu et al. \[2024a,a\]](#), [Singh and Jaggi \[2020\]](#), we propose using optimal transport (OT)-based distance to capture a more nuanced cross-alignment between visual and text domains. Although OT has been explored for prompt learning in natural images and multi-modal learning [Kim et al. \[2023\]](#), [Chen et al. \[2023\]](#), [Nguyen et al. \[2024a\]](#), [Séjourné et al. \[2023\]](#), we are the first to adapt it for whole-slide imaging (WSI), effectively handling the alignment of multi-magnification patches to capture rich structural details across scales.

Recap OT: Given two sets of points (features), we can represent the corresponding discrete distributions as follows:

$$\boldsymbol{\mu} = \sum_{i=1}^M p_i \delta_{f_i}, \quad \boldsymbol{\nu} = \sum_{j=1}^N q_j \delta_{g_j}, \quad (7)$$

where δ_f and δ_g represent Dirac delta functions centered at \mathbf{f} and \mathbf{g} , respectively, and M and N indicate the dimensions of the empirical distribution. The weight vectors $\mathbf{p} = \{p_i\}_{i=1}^M$ and $\mathbf{q} = \{q_j\}_{j=1}^N$ lie within the M and N -dimensional simplex, respectively, meaning they satisfy $\sum_{i=1}^M p_i = 1$ and $\sum_{j=1}^N q_j = 1$. The discrete optimal transport problem can then be expressed as:

$$\begin{aligned} \mathbf{T}^* &= \arg \min_{\mathbf{T} \in \mathbb{R}^{MXN}} \sum_{i=1}^M \sum_{j=1}^N \mathbf{T}_{ij} \mathbf{C}_{ij} \\ \text{s.t.} \quad \mathbf{T} \mathbf{1}^N &= \boldsymbol{\mu}, \quad \mathbf{T}^\top \mathbf{1}^M = \boldsymbol{\nu}. \end{aligned} \quad (8)$$

where \mathbf{T}^* is denoted as the optimal transport plan, which is optimized to minimize the total distance between the two probability vectors, \mathbf{C} is the cost matrix which measures the distance between \mathbf{f}_i and \mathbf{g}_j . We then define the OT distance between $\boldsymbol{\mu}$ and $\boldsymbol{\nu}$ as:

$$d_{\text{OT}}(\boldsymbol{\mu}, \boldsymbol{\nu}) = \langle \mathbf{T}^*, \mathbf{C} \rangle. \quad (9)$$

Objective functions: Given the visual prompt-guided slide features $\mathbf{p}_v^{(l)} \in \mathbb{R}^{N_p \times d}$ in Eq.(6) and the descriptive text prompts $\mathbf{T}^{(l)}$ in Eq.(2), we compute the textual embedding for $\mathbf{T}^{(l)}$ as $\mathbf{p}_t^{(l)} = E_T(\mathbf{T}^{(l)}) \in \mathbb{R}^{M \times d}$. We next denote $\mathbf{T}_c^{(l)}$ as the input text prompts, $(\mathbf{p}_t^{(l)})_c$ as the extracted textual embedding, and $(\mathbf{p}_v^{(l)})_c$ as the visual prompt-guided slide features associated with class c . We then aim to minimize the distance between $\mathbf{T}_c^{(l)}$ and $(\mathbf{p}_v^{(l)})_c$, indicated as $d_{\text{OT}}(\mathbf{T}_c^{(l)}, (\mathbf{p}_v^{(l)})_c)$ in the paper, by computing optimal transport distance between $(\mathbf{p}_t^{(l)})_c$ and $(\mathbf{p}_v^{(l)})_c$. Specifically, we treat $(\mathbf{p}_t^{(l)})_c \rightarrow \mathbf{F} = \{\mathbf{f}_i|_{i=1}^M\}$ and $(\mathbf{p}_v^{(l)})_c \rightarrow \mathbf{G} = \{\mathbf{g}_j|_{j=1}^{N_p}\}$ and compute the cost matrix \mathbf{C} as $\mathbf{C} = (\mathbf{1} - \mathbf{F}^T \mathbf{G}) \in \mathbb{R}^{M \times N_p}$, which used to compute \mathbf{T}^* in Eq. (8) for estimate optimal transport distance defined in Eq. (9). Following the same procedure, we can also compute $d_{\text{OT}}(\mathbf{T}_c^{(h)}, (\mathbf{p}_v^{(h)})_c)$ at high-resolution image patches. Then, the prediction probability is written as:

$$P_c = \frac{\exp(2 - \sum_{k \in \{l, h\}} d_{\text{OT}}(\mathbf{T}_c^{(k)}, (\mathbf{p}_v^{(k)})_c))}{\sum_{c'=1}^C \exp(2 - \sum_{k \in \{l, h\}} d_{\text{OT}}(\mathbf{T}_{c'}^{(k)}, (\mathbf{p}_v^{(k)})_c))}, \quad (10)$$

where λ_k controls contribution of each-resolution. Finally, we can train the model with the cross-entropy as:

$$\mathcal{L}_{\text{class}} = \text{Cross}(P, \text{GT}), \quad (11)$$

with $\text{Cross}(\cdot)$ be the cross-entropy and GT denotes slide-level ground-truth.

The details for solvers of Eq.(9) and a relaxed version with unbalanced optimal transport are presented in Sections (D) and (D.1) in Appendix. Intuitively, using OT, in this case, offers several key advantages over cosine similarity. Pathology images exhibit complex, heterogeneous patterns that can be described from multiple perspectives. OT models these relationships as a distribution, enabling a more holistic alignment that handles variability and incomplete details while reducing

noise from irrelevant prompts. This enhances the model’s ability to generalize to unseen or complex disease cases.

4 Experiments

4.1 Settings

Datasets for contrastive learning. PatchGastricADC22 [Tsuneki and Kanavati \[2022\]](#) consists of approximately 262K patches derived from WSI of H&E-stained gastric adenocarcinoma specimens, each paired with associated diagnostic captions collected from the University of Health and Welfare, Mita Hospital, Japan. QUILT-1M [Ikezogwo et al. \[2024\]](#) includes approximately 653K images and one million pathology image-text pairs, gathered from 1,087 hours of educational histopathology videos presented by pathologists on YouTube. ARCH [Gamper and Rajpoot \[2021\]](#) is a pathology multiple-instance captioning dataset containing pathology images at the bag and tile level. However, our work focuses on tile-level images from all datasets for our contrastive training strategy. In total, we collected approximately 923K images from these datasets.

Downstream tasks. For the classification task, the proposed method was evaluated in three datasets from the Cancer Genome Atlas Data Portal [The Cancer Genome Atlas \(TCGA\)](#): TCGA-NSCLC, TCGA-RCC, and TCGA-BRCA. We followed the ViLa-MIL [Shi et al. \[2024\]](#) experimental settings for TCGA-NSCLC and TCGA-RCC, randomly selecting proportions for training, validation, and testing. For TCGA-BRCA, we adapted the training and testing slide ID from MSCPT [Han et al. \[2024\]](#). The detailed description is included in the appendix section.

Implementation Details. We followed the ViLa-MIL preprocessing pipeline for tissue region selection and patch cropping. To integrate our attention module with CLIP50 and PLIP, we extracted tile-level embeddings from their frozen vision encoders (1024-dimensional for CLIP50 and 512 for PLIP). We used the visual encoder of Prov-GigaPath to produce 1536-dimensional embeddings. To align it with PLIP’s frozen text encoder, we developed two MLP-based adaptors that project both encoders into a shared feature space during a contrastive learning process, using datasets outlined in Section 4.

Table 1: Comparison of methods on TCGA-BRCA with few-shot settings. Results are shown for AUC, F1, and Accuracy (ACC). FVM denotes for foundation vision-language models.

	Methods	# Param.	TCGA-BRCA		
			AUC	F1	ACC
CLIP ImageNet Pretrained	Max-pooling	197K	60.42±4.35	56.40±3.58	68.55±6.54
	Mean-pooling	197K	66.64±4.21	60.70±2.78	71.73±3.59
	ABMIL Ilse et al. [2018]	461K	69.24±3.90	61.72±3.36	72.77±3.15
	CLAM-SB Lu et al. [2021]	660K	67.80±5.14	60.51±5.01	72.46±4.36
	CLAM-MB Lu et al. [2021]	660K	60.81±4.87	55.48±4.96	67.31±4.19
	TransMIL Shao et al. [2021]	2.54M	65.62±3.20	60.75±4.04	67.52±4.16
	DSMIL Li et al. [2021]	462K	66.18±3.08	59.35±3.18	67.52±1.56
	RRT-MIL Tang et al. [2024]	2.63M	66.33±4.30	61.14±5.93	71.21±8.94
	CoOp Zhou et al. [2022b]	337K	68.86±4.35	61.64±2.40	71.08±3.22
	CoCoOp Zhou et al. [2022a]	370K	69.13±4.27	61.48±2.62	72.41±1.87
	Metaprompt Zhao et al. [2024]	360K	69.12±4.46	63.39±4.38	74.65±7.20
	TOP Qu et al. [2024a]	2.11M	69.74±3.14	63.39±4.62	74.41±5.27
	ViLa-MIL Shi et al. [2024]	2.77M	72.25±6.16	62.04±2.38	75.01±6.14
	MSCPT Han et al. [2024]	1.35M	74.56±4.54	65.59±1.85	75.82±2.38
FVM	MGPATH (ViT)	592K	74.96±6.98	64.60±5.39	77.10±2.39
	CONCH Lu et al. [2024]	110M	84.11±15.44	65.63±10.81	73.24±8.89
PLIP Pathology Pretrained	CONCH Lu et al. [2024]	110M	84.11±15.44	65.63±10.81	73.24±8.89
	QUILT Ikezogwo et al. [2024]	63M	73.48±10.57	63.78±8.72	73.26±10.13
	Max-pooling	197K	66.50±2.74	61.50±2.88	71.57±4.82
	Mean-pooling	197K	71.62±2.41	66.34±2.96	74.45±2.49
	ABMIL Ilse et al. [2018]	461K	72.41±4.25	63.04±3.62	74.09±4.38
	CLAM-SB Lu et al. [2021]	660K	72.34±6.17	65.51±3.28	76.16±4.36
	CLAM-MB Lu et al. [2021]	660K	73.41±3.76	66.11±1.94	77.88±2.30
	TransMIL Shao et al. [2021]	2.54M	74.98±6.01	67.50±6.00	77.04±6.14
	DSMIL Li et al. [2021]	462K	71.44±2.72	64.48±1.64	75.26±2.28
	RRT-MIL Tang et al. [2024]	2.63M	71.21±6.46	64.15±1.38	75.92±5.10
	CoOp Zhou et al. [2022b]	337K	71.53±2.45	64.84±2.40	74.22±5.02
	CoCoOp Zhou et al. [2022a]	370K	72.65±4.63	66.63±3.55	66.98±3.35
	Metaprompt Zhao et al. [2024]	360K	74.86±4.25	65.03±1.81	77.88±3.22
	TOP Qu et al. [2024a]	2.11M	76.13±6.01	66.55±1.72	78.58±5.30
	ViLa-MIL Shi et al. [2024]	2.77M	74.06±4.62	66.03±1.81	78.12±4.88
	MSCPT Han et al. [2024]	1.35M	75.55±5.25	67.46±2.43	79.14±2.63
	MGPATH	592K	<u>79.02±6.43</u>	<u>68.25±4.42</u>	79.65±1.72
	MGPATH (PLIP-G)	5.35M	87.36±1.85	73.13±3.49	<u>79.56±4.77</u>

To implement spatial attention, we use a Graph Attention Network (GAT) to model spatial relationships between WSI patches. Each tile-level embedding serves as a node, connected to its left, right, top, and bottom neighbors, ensuring local spatial dependencies are captured. We then integrate spatial patch group-based attention $\mathbf{p}_{v,gr}$ into patch-based attention $\mathbf{p}_{v,p}$ using Equation 6. The hyperparameter α (0 to 1) controls the balance between spatial context and prototype-based

guidance.

4.2 Comparison to State-of-the-Art

We compare our MGPath with state-of-the-art multi-instance learning methods, including Maxpooling, Mean-

pooling, ABMIL Ilse et al. [2018], CLAM Lu et al. [2021], TransMIL Shao et al. [2021], DSMIL Li et al. [2021], GTMIL Zheng et al. [2022], DTMIL Zhang et al. [2022a], RRT-MIL Tang et al. [2024] and IBMIL Lin et al. [2023], and vision-language methods, including CoOp Zhou et al. [2022b], CoCoOp Zhou et al. [2022a], Metaprompt Zhao et al. [2024], TOP Qu et al. [2024a], ViLa-MIL Shi et al. [2024], MSCPT Han et al. [2024], QUILT Ikezogwo et al. [2024], CONCH Lu et al. [2024]. Among these, QUILT and CONCH are foundation VLMs.

We provide different versions for our MGPath including CLIP backbone ReNet-50 (CLIP50) for TCGA-NSCLC and TCGA-RCC and ViT-16 backbone for TCGA-BRCA. We also provide a version using PLIP backbone, as well as GigaPath-PLIP, which was pre-trained on the Pathology dataset.

4.3 Results on Few-shot and Zero-shot Settings.

MGPath with CLIP and PLIP backbones outperform several competitive MIL and VLM methods. As shown in Tables 2 and 1, our MGPath, based on CLIP50 and PLIP, outperforms several baseline models and achieves significant improvements over other VLMs with similar architectures, such as ViLa and MSCPT. The performance gain is particularly notable with the PLIP backbone. For example, on TCGA-BRCA using CLIP (ViT), MGPath achieves an accuracy of 77.10%, compared to 75.82% for MSCPT and 75.01% for ViLA-MIL. Additionally, with the PLIP backbone, MGPath surpasses MSCPT and ViLa-MIL by margins of approximately 3.5% to 5%.

GigaPath-PLIP is a strong pre-trained VLM. We validated our whole-slide vision foundation model, pre-trained on 1.3 billion pathology images, using the PLIP text encoder. By incorporating pathology-specific features from Prov-GigaPath Xu et al. [2024], the integrated MGPath (PLIP-G) model demonstrated strong performance across multiple metrics on the TCGA-NSCLC, TCGA-RCC, and TCGA-BRCA datasets. When compared to other foundation VLMs such as CONCH and QUILT, our model consistently outperforms them. For example, we achieve a 3% improvement in AUC over CONCH on both the TCGA-BRCA and TCGA-NSCLC datasets.

GigaPath-PLIP achieves competitive performance in zero-shot tasks. We evaluate the zero-shot capabilities of our model on three datasets and compare its performance against foundation VLMs such as CONCH, QUILT, and PLIP. The results, summarized in Table 3, show that the proposed VLM model achieves the best average performance across datasets, followed by CONCH and PLIP. This consistent top-tier performance across multiple benchmarks underscores the robustness and generalizability of our model.

4.4 Ablation Studies

PLIP enhanced Prov-GigaPath. We validate the use of Prov-GigaPath and PLIP under the following settings: (i) using full vision-language PLIP model; (ii) combining Prov-GigaPath with PLIP through the MLP layer which was pre-trained on the large-scale dataset; (iii) integrating Prov-GigaPath with PLIP through adaptor layers which were randomly initialized; (iv) utilizing Prov-GigaPath and an adaptor layer to map to the class output and only train MLP and last FFN

Table 2: Comparison of methods on TCGA-NSCLC, and TCGA-RCC datasets with few-shot settings. Results are shown for AUC, F1, and Accuracy (ACC).

Methods	# Param.	TCGA-NSCLC			TCGA-RCC		
		AUC	F1	ACC	AUC	F1	ACC
Max-pooling	197K	53.0±6.0	45.8±8.9	53.3±3.4	67.4±4.9	46.7±11.6	54.1±4.8
Mean-pooling	197K	67.4±7.2	61.1±5.5	61.9±5.5	83.3±6.0	60.9±8.5	62.3±7.4
ABMIL Ilse et al. [2018]	461K	60.5±15.9	56.8±11.8	61.2±6.1	83.6±3.1	64.4±4.2	65.7±4.7
CLAM-SB Lu et al. [2021]	660K	66.7±13.6	59.9±13.8	64.0±7.7	90.1±2.2	75.3±7.4	77.6±7.0
CLAM-MB Lu et al. [2021]	660K	68.8±12.5	60.3±11.1	63.0±9.3	90.9±4.1	76.2±4.4	78.6±4.9
TransMIL Shao et al. [2021]	2.54M	64.2±8.5	57.5±6.4	59.7±5.4	89.4±5.6	73.0±7.8	75.3±7.2
DSMIL Li et al. [2021]	462K	67.9±8.0	61.0±7.0	61.3±7.0	87.6±4.5	71.5±6.6	72.8±6.4
GTMIL Zheng et al. [2022]	N/A	66.0±15.3	61.1±12.3	63.8±9.9	81.1±13.3	71.1±15.7	76.1±12.9
DTMIL Zhang et al. [2022a]	986.7K	67.5±10.3	57.3±11.3	66.6±7.5	90.0±4.6	74.4±5.3	76.8±5.2
IBMIL Lin et al. [2023]	N/A	69.2±7.4	57.4±8.3	66.9±6.5	90.5±4.1	75.1±5.2	77.2±4.2
ViLa-MIL Shi et al. [2024]	8.8M/47M	74.7±3.5	67.0±4.9	67.7±4.4	92.6±3.0	78.3±6.9	80.3±6.2
CONCH (Lu et al. [2024])	110M	89.46±10.2	78.5±9.31	78.78±9.1	88.08±4.59	78.21±4.2	71.67±19.4
QUILT Ikezogwo et al. [2024]	63M	79.66±13.19	72.30±13.35	72.42±13.24	96.92±1.6	78.46±5.55	86.34±1.56
MGPath (CLIP)	1.6M/39M	77.2±1.3	70.9±2.0	71.0±2.1	92.1 ± 2.8	76.5 ± 5.2	81.7 ± 2.9
MGPath (PLIP)	592K	83.6 ± 4.5	76.41 ± 4.8	76.5 ± 4.8	94.7 ± 1.6	78.6 ± 4.9	83.6 ± 3.5
MGPath (PLIP-G)	5.35M	93.02±2.99	84.64±4.75	84.77±4.67	98.2±0.31	88.33±3.41	91.72±1.74

Table 3: Zero-shot classification performance on TCGA-NSCLC, TCGA-RCC, and TCGA-BRCA datasets. Metrics reported include balanced accuracy (B-Acc) and weighted F1-score (W-F1).

Zero-shot	TCGA-NSCLC		TCGA-RCC		TCGA-BRCA		Average	
	B-Acc	W-F1	B-Acc	W-F1	B-Acc	W-F1	B-Acc	W-F1
QuiltNet	61.3	56.1	59.1	51.8	51.3	40.1	57.23	49.33
CONCH	80.0	79.8	72.9	69.1	64.0	61.2	72.3	70.03
PLIP	70.0	68.5	50.7	46.0	64.7	63.8	61.8	59.43
PLIP-G (Our)	72.7	72.6	81.3	81.4	70.0	69.9	74.67	74.63

layer of slide encoder; (v) only using **Prov-GigaPath** and an MLP layer to map to the class output and train MLP, the query matrix of last layer and the last FFN layer of slide encoder. Table 5 shows that using **Prov-GigaPath** combined with PLIP boosts the final performance compared to only using PLIP or **Prov-GigaPath**.

Table 4: Ablation studies on multi-granular (M-Gran), ratio combines two attention levels (α), and message passing network types.

Configurations	TCGA-NSCLC		
	AUC	F1	ACC
MGPATH (CLIP)	76.2 \pm 2.2	69.0 \pm 3.5	69.3 \pm 2.8
- w/o M-Gran (CLIP)	74.6 \pm 2.2	67.8 \pm 2.4	67.8 \pm 2.5
MGPATH (PLIP-G)	91.7 \pm 3.6	84.2 \pm 4.6	84.4 \pm 4.5
- w/o M-Gran (PLIP-G)	90.6 \pm 4.5	82.4 \pm 5.7	82.5 \pm 5.7
MGPATH, $\alpha = 0.2$	76.2 \pm 2.2	69.0 \pm 3.5	69.3 \pm 2.8
- $\alpha = 0.5$	73.7 \pm 3.1	67.4 \pm 2.6	67.8 \pm 2.7
- $\alpha = 0.8$	72.2 \pm 5.2	66.4 \pm 5.5	66.8 \pm 5.2
TCGA-RCC			
MGPATH (CLIP)	92.1 \pm 2.8	76.5 \pm 5.2	81.7 \pm 2.9
- w/o M-Gran (CLIP)	91.6 \pm 3.5	72.3 \pm 6.4	80.2 \pm 4.4
MGPATH (PLIP-G)	98.1 \pm 0.6	85.7 \pm 1.1	89.9 \pm 2.0
- w/o M-Gran (PLIP-G)	98.1 \pm 0.6	85.0 \pm 4.0	89.3 \pm 3.0

Table 5: Ablation studies on adaptor learning for Prov-GiGaPath and PLIP. PLIP-G denotes for mixed version between Prov-GiGaPath and PLIP.

Methods	# Param.	TCGA-NSCLC		
		AUC	F1	ACC
MGPATH (PLIP)	592K	83.6 \pm 4.5	76.41 \pm 4.8	76.5 \pm 4.8
MGPATH (PLIP-G)	5.35M	91.7 \pm 3.6	84.2 \pm 4.6	84.4 \pm 4.5
MGPATH Random Adaptors	5.35M	91.4 \pm 4.2	82.8 \pm 5.7	83.0 \pm 5.6
GiGaPath Tuning (MLP + last FFN)	4.7M	62.7 \pm 3.5	64.66 \pm 5.3	52.8 \pm 3.4
GiGaPath Tuning (MLP + last Q-ViT)	5.8M	83.1 \pm 6.9	74.3 \pm 7.5	75.8 \pm 6.1

Table 6: Contribution of OT and multiple descriptive text prompts

Methods	TCGA-NSCLC		
	AUC	F1	ACC
MGPATH (OT, 4 text prompts)	76.2 \pm 2.2	69.0 \pm 3.5	69.3 \pm 2.8
MGPATH (OT, 2 text prompts)	77.2 \pm 1.3	70.9 \pm 2.0	71.0 \pm 2.1
MGPATH (Cosine, 2 text prompts)	75.8 \pm 3.7	68.3 \pm 4.5	68.4 \pm 4.5
TCGA-RCC			
MGPATH (OT, 4 text prompts)	92.1 \pm 2.8	76.5 \pm 5.2	81.7 \pm 2.9
MGPATH (OT, 2 text prompts)	92.1 \pm 2.6	75.6 \pm 3.9	80.4 \pm 2.4
MGPATH (Cosine, 4 text prompts)	91.8 \pm 2.8	75.9 \pm 4.3	80.5 \pm 2.6

Multi-Granular Prompt Learning. In Table 4, we show the performance of MGPATH with and without multi-granular (M-Gran) for CLIP (row 1 and 2) and PLIP-G (row 3 and 4) on TCGA-NSCLC dataset. It shows that using M-Gran improves the final performance of MGPATH. This also happens on TCGA-RCC dataset. Table 4 also shows the impact of ratio when combining attention with graph and attention no graph on TCGA-NSCLC. It shows that with a ratio of 0.2/0.8 (0.2 for spatial attention obtained from graph structure and 0.8 for prototype-guided attention), MGPATH achieves the highest performance.

OT as Alignment between Contextual Prompts. Table 6 validates the use of OT in our MGPATH on TCGA-NSCLC and TCGA-RCC. We see that using OT helps to boost the performance of MGPATH (rows 1 and 2) compared to the use of cosine (rows 3 and 4). It also shows that the number of prompt vectors depends on each dataset. In the appendix, we also run with another version using unbalanced optimal transport (UoT). We observe that both UoT and OT provide good alignment quality, with UoT slightly outperforming OT. However, this advantage comes at the cost of increased running time.

4.5 Discussion

While we demonstrate significant improvements in few-shot and zero-shot WSI classification across several settings, this paper does not explore other important challenges. For example, how can we scale the current attention mechanism to handle even larger image patches (e.g., using Flash Attention [\[Dao et al. 2022\]](#)), or extend the model from classification to tumor segmentation tasks [\[Khened et al. 2021\]](#). Additionally, the potential for extending GiGaPath to integrate with other large-scale VLM models, such as CONCH [\[Lu et al. 2024\]](#), remains unexplored.

5 Conclusion

High-resolution WSI is crucial for cancer diagnosis and treatment but presents challenges in data analysis. Recent VLM approaches, which utilize few-shot and weakly supervised learning, have shown promise in handling complex whole-slide pathology images with limited annotations. However, many overlook the hierarchical relationships between visual and textual embeddings, ignoring the connections between global and local pathological details or relying on non-pathology-specific pre-trained models like CLIP. Additionally, previous metrics lack precision in capturing fine-grained alignments between image-text pairs. To address these gaps, (i) we propose **MGPATH**, which integrates **Prov-GigaPath** with **PLIP**, cross-aligning them with 923K domain-specific image-text pairs. (ii) Our multi-granular prompt learning approach captures hierarchical tissue details effectively, (iii) while OT-based visual-text distance ensures robustness against data augmentation perturbations. Extensive experiments on three cancer subtyping datasets demonstrate that **MGPATH** achieves state-of-the-art results in WSI classification. We expect that this work will pave the way for combining large-scale domain-specific models with multi-granular prompt learning and optimal transport to enhance few-shot learning in pathology.

6 Acknowledgement

This work is supported in part by funds from the German Ministry of Education and Research (BMBF) under grant agreements *No. 01D2208A* and *No. 01KD2414A* (project FAIrPaCT).

The project “Development of an intelligent collaboration service for AI-based collaboration between rescue services and central emergency rooms” (acronym: CONNECT_ED) is funded by the German Federal Ministry of Education and Research under grant number *16SV8977* and by the joint project *KISSKI* under grant number *1IS22093E*.

The authors gratefully acknowledge the computing time granted by the Resource Allocation Board and provided on the supercomputer Emmy/Grete at NHR-Nord@Göttingen as part of the NHR infrastructure. The calculations for this research were conducted with computing resources under the project *nim00014*.

The authors gratefully acknowledge the computing time granted by the KISSKI project. The calculations for this research were conducted with computing resources under the project *kisski-umg-fairpact-2*.

The authors thank the International Max Planck Research School for Intelligent Systems (IMPRS-IS) for supporting Duy M. H. Nguyen. Duy M. H. Nguyen and Daniel Sonntag are also supported by the XAINES project (BMBF, *01IW20005*), No-IDLE project (BMBF, *01IW23002*), and the Endowed Chair of Applied Artificial Intelligence, Oldenburg University.

Supplement to “MGPATH: Vision-Language Model with Multi-Granular Prompt Learning for Few-Shot WSI Classification”

A Description of Dataset Splitting

TCGA-BRCA. This dataset contains 1056 whole slide images of breast invasive carcinoma. To conduct fair experiments, we adapted training and testing slides provided by the GitHub repository of MSCPT [Han et al. \[2024\]](#). In the MSCPT setup, 20% of the dataset was allocated for training, while the remaining 80% (833 slides) served as the test set. A fixed set of 16-shot WSIs was randomly sampled from the training set. Additionally, MSCPT specified the exact training and testing slides used in its experiments. However, there are 35 slides in which we got errors in the pre-processing steps; thus, we replaced those slides with the other ones (same number of WSI per class) downloaded from Cancer Genome Atlas (TCGA) Data Portal (GDC) [The Cancer Genome Atlas \(TCGA\)](#).

TCGA-RCC & TCGA-NSCLC. We adopt the same data splitting as in ViLa-MIL [Shi et al. \[2024\]](#), using 16-shot samples for training in each dataset. For testing, 192 samples were used for TCGA-RCC and 197 samples were used for TCGA-NSCLC.

A.1 Other hyper-parameters

For all experiments, we trained MGPATH with the Adam optimizer with a learning rate of 9×10^{-6} and a weight decay of 1×10^{-5} to fine-tune all versions of MGPATH presented in Tables 1 and 2. The training process was conducted for a maximum of 200 epochs, with a batch size set to 1. The best checkpoints are picked based validation performance with F1 score.

A.2 Baseline Setups

TCGA-BRCA: The baselines in [Table 1](#) are sourced from the MSCPT [Han et al. \[2024\]](#) paper, where various methods are evaluated using two backbones: Vision Transformer (ViT) [Alexey \[2020\]](#) from the CLIP model (top section of [Table 1](#)) and PLIP [Huang et al. \[2023\]](#) (bottom section of [Table 1](#)). In this context, we introduce three variations of MGPATH - ViT, PLIP, and GigaPath-PLIP (abbreviated as PLIP-G), where all versions utilize frozen vision and text encoders.

TCGA-RCC & TCGA-NSCLC: The baselines in [Table 2](#) are adapted from ViLa-MIL [Shi et al. \[2024\]](#) where methods employ ResNet-50 from the CLIP model as the primary backbone. We present MGPATH results using three architectures: ResNet-50, PLIP, and PLIP-G. With ResNet-50, we follow the ViLa-MIL approach by training the text encoder and reporting performance for this setup. To assess efficiency, we provide the total parameter counts for both ViLa-MIL and MGPATH, considering scenarios with frozen backbones and trainable text encoders. For PLIP and PLIP-G, all visual and text encoders are kept frozen.

CONCH & QUILT: We download the pre-trained weights of these foundation models and adapt them for zero-shot evaluation on TCGA datasets following the authors’ guidelines from [Lu et al. \[2024\]](#), which randomly sample 75 samples for each class. For few-shot settings, since official implementations are not provided, we initialize the models with their pre-trained weights and allow fully fine-tune the text encoder and evaluate on the same subsets that we use for other baselines. While CONCH

provides prompts for the datasets in its publication, QUILT does not. Therefore, we fine-tune the model using CONCH’s prompts and our own generated prompts for QUILT.

Table 7: Comparison of message passing algorithms in MGPATH, including GAT-CONV, Graph Isomorphism Network (GIN), and Graph Convolutional Network (GCN). Performance is evaluated on the TCGA-NSCLC dataset using 5-fold cross-validation.

Configurations	TCGA-NSCLC		
	AUC	F1	ACC
MGPATH (GAT CONV)	77.2 \pm 1.3	70.9 \pm 2.0	71.0 \pm 2.1
MGPATH (GIN)	77.1 \pm 2.9	69.8 \pm 3.9	69.9 \pm 4.0
MGPATH (GCN)	75.1 \pm 2.9	67.6 \pm 2.5	67.1 \pm 2.8

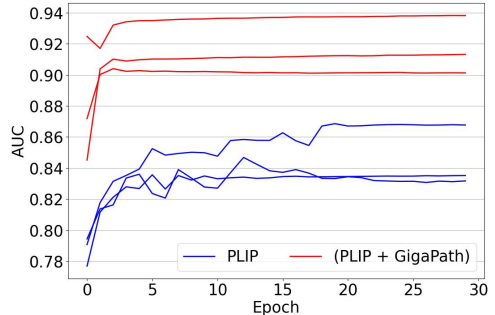


Figure 4: AUC performance comparison over epochs for PLIP (blue) and PLIP combined with GigaPath (red). GigaPath significantly enhances the AUC, achieving more stable and higher values, particularly in the early epochs.

B Impact of PLIP enhanced Prov-GigaPath

Figure 4 presents the AUC curves for three randomly selected folds, illustrating the impact of Prov-GigaPath on model performance. The results show that integrating Prov-GigaPath leads to consistently higher AUC values across all folds, demonstrating its effectiveness in enhancing the proposed model. Notably, the improvements are most pronounced during the early training epochs, where the model converges faster and achieves more stable performance compared to the baseline. This suggests that Prov-GigaPath facilitates better feature extraction and generalization, ultimately leading to a more robust model.

C Ablation Study on Message Passing Networks

In Table 7, we evaluate the performance of MGPATH (CLIP) using the Graph Attention Network (GAT-CONV) against alternatives like the Graph Isomorphism Network (GIN) Xu et al. [2019b] and the Graph Convolutional Network (GCN) Kipf and Welling [2017]. The results show that MGPATH (GIN) achieves comparable performance to MGPATH (GAT-CONV), however, with higher variance. In contrast, MGPATH (GAT-CONV) significantly outperforms the GCN-based version, likely due to GAT’s ability to dynamically assign attention weights to neighboring image patches, enabling it to prioritize the most relevant neighbors for each node.

D Additional Details on Optimal Transport Distance

The following paragraphs will provide detailed information on the implementation of (un-balanced) optimal transport (OT) Villani et al. [2009], Peyré et al. [2019] and specifically the alignment of prompt-guided visual-text distances in MGPATH.

D.1 OT Formulation and Efficient Solver

Given two set of feature embeddings $\mathbf{F} = \{\mathbf{f}_i|_{i=1}^M\} \in \mathbb{R}^{M \times d}$ and $\mathbf{G} = \{\mathbf{g}_j|_{j=1}^N\} \in \mathbb{R}^{N \times d}$, we can represent them as two discrete distributions $\boldsymbol{\mu}$ and $\boldsymbol{\nu}$ by:

$$\boldsymbol{\mu} = \sum_{i=1}^M p_i \delta_{\mathbf{f}_i}, \quad \boldsymbol{\nu} = \sum_{j=1}^N q_j \delta_{\mathbf{g}_j}, \quad (12)$$

where $\delta_{\mathbf{f}_i}$ and $\delta_{\mathbf{g}_j}$ represent Dirac delta functions centered at \mathbf{F} and \mathbf{G} , respectively and the weights are elements of the marginal $\mathbf{p} = \{p_i\}_{i=1}^M$ and $\mathbf{q} = \{q_j\}_{j=1}^N$ and can be selected as the uniform weight with $\sum_{i=1}^M p_i = 1$, $\sum_{j=1}^N q_j = 1$.

Then we can compute the distance between \mathbf{F} and \mathbf{G} through $\boldsymbol{\mu}$ and $\boldsymbol{\nu}$ (Eq.(9)) as

$$d_{\text{OT}}(\boldsymbol{\mu}, \boldsymbol{\nu}) = \langle \mathbf{T}^*, \mathbf{C} \rangle. \quad (13)$$

where

$$\begin{aligned} \mathbf{T}^* &= \arg \min_{\mathbf{T} \in \mathbb{R}^{M \times N}} \sum_{i=1}^M \sum_{j=1}^N \mathbf{T}_{ij} \mathbf{C}_{ij} \\ \text{s.t. } \mathbf{T} \mathbf{1}^N &= \boldsymbol{\mu}, \quad \mathbf{T}^\top \mathbf{1}^M = \boldsymbol{\nu}. \end{aligned} \quad (14)$$

with $\mathbf{C} \in \mathbb{R}^{M \times N}$ is the cost matrix which measures the distance between $\mathbf{f}_i \in \boldsymbol{\mu}$ and $\mathbf{g}_j \in \boldsymbol{\nu}$.

Because directly solving Eq (14) is high-computational costs ($O(n^3 \log n)$ with n proportional to M and N), Sinkhorn algorithm [Cuturi \[2013\]](#) is proposed to approximate solution by solving a regularized problem:

$$\begin{aligned} \mathbf{T}^* &= \arg \min_{\mathbf{T} \in \mathbb{R}^{M \times N}} \sum_{i=1}^M \sum_{j=1}^N \mathbf{T}_{ij} \mathbf{C}_{ij} - \lambda H(\mathbf{T}) \\ \text{s.t. } \mathbf{T} \mathbf{1}^N &= \boldsymbol{\mu}, \quad \mathbf{T}^\top \mathbf{1}^M = \boldsymbol{\nu}. \end{aligned} \quad (15)$$

where $H(\mathbf{T}) = \sum_{ij} \mathbf{T}_{ij} \log \mathbf{T}_{ij}$ be an entropy function and $\lambda > 0$ is the regularization parameter. The optimization problem in Eq. (15) is strictly convex, allowing us to achieve a solution efficiently with fewer iterations as outlined below:

$$\mathbf{T}^* = \text{diag}(\mathbf{a}^t) \exp(-\mathbf{C}/\lambda) \text{diag}(\mathbf{b}^t) \quad (16)$$

where t is the iteration and $\mathbf{a}^t = \boldsymbol{\mu} / \exp(-\mathbf{C}/\lambda) \mathbf{b}^{t-1}$ and $\mathbf{b}^t = \boldsymbol{\nu} / \exp(-\mathbf{C}/\lambda) \mathbf{a}^t$, with the initialization on $\mathbf{b}^0 = \mathbf{1}$. In our experiments, we used $t = 100$ and $\lambda = 0.1$ based on validation performance.

D.2 Relaxed Marginal Constraints with Unbalanced Optimal Transport

Due to strict marginal constraints in Eq (14), optimal transport may be unrealistic in real-world scenarios where data distributions are noisy, incomplete, or unbalanced. The Unbalanced Optimal Transport (UoT) [Chizat et al. \[2018\]](#), [Liero et al. \[2018\]](#) addresses this challenge by relaxing the marginal constraints, allowing for partial matching through penalties on mass creation or destruction. In particular, UoT solves

$$\mathbf{T}^* = \arg \min_{\mathbf{T} \in \mathbb{R}^{M \times N}} \sum_{i=1}^M \sum_{j=1}^N \mathbf{T}_{ij} \mathbf{C}_{ij} - \lambda H(\mathbf{T}) \quad (17)$$

$$+ \rho_1 \text{KL}(\mathbf{T}\mathbf{1}^N \parallel \boldsymbol{\mu}) + \rho_1 \text{KL}(\mathbf{T}^\top \mathbf{1}^M \parallel \boldsymbol{\nu})$$

here, ρ_1 and ρ_2 represent the marginal regularization parameters, and $\text{KL}(\mathbf{P} \parallel \mathbf{Q})$ denotes the Kullback-Leibler divergence between two positive vectors. Similar to the classical OT formulation, there are solvers based on the Sinkhorn algorithm that can address Eq. (18) [Pham et al. \[2020\]](#). However, these solvers typically require more iteration steps to converge to optimal solutions due to the added complexity introduced by the relaxed marginal constraints.

E Unbalance Optimal Transport (UoT)

Table 8: MGPATH performance and running time (in second) comparison between OT and UoT.

Methods	TCGA-NSCLC			
	AUC \uparrow	F1 \uparrow	ACC \uparrow	Time (s) \downarrow
MGPATH (OT, 4 text prompts)	76.2 \pm 2.2	69.0 \pm 3.5	69.3 \pm 2.8	1482
MGPATH (UoT, 4 text prompts)	77.0 \pm 1.8	70.2 \pm 3.4	70.4 \pm 3.3	3260
TCGA-RCC				
MGPATH (OT, 4 text prompts)	92.1 \pm 2.8	76.5 \pm 5.2	81.7 \pm 2.9	1451
MGPATH (UoT, 4 text prompts)	92.8 \pm 2.4	76.8 \pm 4.7	82.4 \pm 2.4	3049

To conduct a comparative evaluation of the performance of MGPATH using optimal transport versus unbalanced optimal transport (Section D.2) given the more flexible constraints in UoT, we conducted an additional experiment. To be specific, we test on the TCGA-NSCLC and TCGA-RCC datasets with the CLIP architecture (ResNet-50) using a 4-text-prompt setting. Table 8 presents our findings where the running time is computed as seconds of average across five-folds. The results show that UoT outperforms OT with an approximate 1% improvement across all metrics. However, UoT is approximately 2 times slower than OT. This increase is attributed to the added flexibility and complexity introduced by relaxing the marginal constraints in the UoT formulation. Given this trade-off, we choose OT as the main distance in MGPATH and leave the UoT version for further evaluation. It is also important to know that our OT formulation leverages approximate solutions through the regularized formulation (Eq.,(15)) and produces smoothed optimal mappings \mathbf{T}^* , which can implicitly help the model adapt to perturbations like UoT.

References

F. Ahmed, A. Sellergren, L. Yang, S. Xu, B. Babenko, A. Ward, N. Olson, A. Mohtashamian, Y. Matias, G. S. Corrado, et al. Pathalign: A vision-language model for whole slide images in histopathology. *arXiv preprint arXiv:2406.19578*, 2024. (Cited on page 2.)

D. Alexey. An image is worth 16x16 words: Transformers for image recognition at scale. *arXiv preprint arXiv: 2010.11929*, 2020. (Cited on page 16.)

J. Barker, A. Hoogi, A. Depeursinge, and D. L. Rubin. Automated classification of brain tumor type in whole-slide digital pathology images using local representative tiles. *Medical image analysis*, 30: 60–71, 2016. (Cited on page 2.)

Q. Cao, Z. Xu, Y. Chen, C. Ma, and X. Yang. Domain-controlled prompt learning. In *Proceedings of the AAAI Conference on Artificial Intelligence*, volume 38, pages 936–944, 2024. (Cited on page 3.)

G. Chen, W. Yao, X. Song, X. Li, Y. Rao, and K. Zhang. Plot: Prompt learning with optimal transport for vision-language models. *International Conference on Learning Representations*, 2023. (Cited on pages 3 and 8.)

R. J. Chen, M. Y. Lu, M. Shaban, C. Chen, T. Y. Chen, D. F. Williamson, and F. Mahmood. Whole slide images are 2d point clouds: Context-aware survival prediction using patch-based graph convolutional networks. In *Medical Image Computing and Computer Assisted Intervention-MICCAI 2021: 24th International Conference, Strasbourg, France, September 27–October 1, 2021, Proceedings, Part VIII 24*, pages 339–349. Springer, 2021. (Cited on page 4.)

R. J. Chen, T. Ding, M. Y. Lu, D. F. Williamson, G. Jaume, A. H. Song, B. Chen, A. Zhang, D. Shao, M. Shaban, et al. Towards a general-purpose foundation model for computational pathology. *Nature Medicine*, 30(3):850–862, 2024. (Cited on page 4.)

S. Cheng, S. Liu, J. Yu, G. Rao, Y. Xiao, W. Han, W. Zhu, X. Lv, N. Li, J. Cai, et al. Robust whole slide image analysis for cervical cancer screening using deep learning. *Nature communications*, 12 (1):5639, 2021. (Cited on page 2.)

L. Chizat, G. Peyré, B. Schmitzer, and F.-X. Vialard. Scaling algorithms for unbalanced optimal transport problems. *Mathematics of Computation*, 87(314):2563–2609, 2018. (Cited on page 18.)

M. Cuturi. Sinkhorn distances: Lightspeed computation of optimal transport. *Advances in neural information processing systems*, 26, 2013. (Cited on page 18.)

T. Dao, D. Fu, S. Ermon, A. Rudra, and C. Ré. Flashattention: Fast and memory-efficient exact attention with io-awareness. *Advances in Neural Information Processing Systems*, 35:16344–16359, 2022. (Cited on page 14.)

S. Dong, Z. Pan, Y. Fu, D. Xu, K. Shi, Q. Yang, Y. Shi, and C. Zhuo. Partial unbalanced feature transport for cross-modality cardiac image segmentation. *IEEE Transactions on Medical Imaging*, 42(6):1758–1773, 2023. (Cited on page 3.)

N. Farahani, A. V. Parwani, and L. Pantanowitz. Whole slide imaging in pathology: advantages, limitations, and emerging perspectives. *Pathology and Laboratory Medicine International*, pages 23–33, 2015. (Cited on page 2.)

M. Gadermayr and M. Tschuchnig. Multiple instance learning for digital pathology: A review of the state-of-the-art, limitations & future potential. *Computerized Medical Imaging and Graphics*, page 102337, 2024. (Cited on page 2.)

J. Gamper and N. Rajpoot. Multiple instance captioning: Learning representations from histopathology textbooks and articles. In *Proceedings of the IEEE/CVF conference on computer vision and pattern recognition*, pages 16549–16559, 2021. (Cited on pages 3 and 10.)

P. Gao, S. Geng, R. Zhang, T. Ma, R. Fang, Y. Zhang, H. Li, and Y. Qiao. Clip-adapter: Better vision-language models with feature adapters. *International Journal of Computer Vision*, 132(2): 581–595, 2024. (Cited on pages 2 and 3.)

C. Ge, R. Huang, M. Xie, Z. Lai, S. Song, S. Li, and G. Huang. Domain adaptation via prompt learning. *IEEE Transactions on Neural Networks and Learning Systems*, 2023. (Cited on page 5.)

M. Han, L. Qu, D. Yang, X. Zhang, X. Wang, and L. Zhang. Mscpt: Few-shot whole slide image classification with multi-scale and context-focused prompt tuning. *arXiv preprint arXiv:2408.11505*, 2024. (Cited on pages 2, 3, 4, 6, 7, 10, 11, 12, and 16.)

Z. Huang, F. Bianchi, M. Yuksekgonul, T. J. Montine, and J. Zou. A visual–language foundation model for pathology image analysis using medical twitter. *Nature medicine*, 29(9):2307–2316, 2023. (Cited on pages 2, 3, 4, and 16.)

W. Ikezogwo, S. Seyfioglu, F. Ghezloo, D. Geva, F. Sheikh Mohammed, P. K. Anand, R. Krishna, and L. Shapiro. Quilt-1m: One million image-text pairs for histopathology. *Advances in neural information processing systems*, 36, 2024. (Cited on pages 2, 3, 4, 10, 11, 12, and 13.)

M. Ilse, J. Tomczak, and M. Welling. Attention-based deep multiple instance learning. In *International conference on machine learning*, pages 2127–2136. PMLR, 2018. (Cited on pages 2, 4, 7, 11, 12, and 13.)

M. U. Khattak, H. Rasheed, M. Maaz, S. Khan, and F. S. Khan. Maple: Multi-modal prompt learning. In *Proceedings of the IEEE/CVF Conference on Computer Vision and Pattern Recognition*, pages 19113–19122, 2023. (Cited on page 5.)

M. Khened, A. Kori, H. Rajkumar, G. Krishnamurthi, and B. Srinivasan. A generalized deep learning framework for whole-slide image segmentation and analysis. *Scientific reports*, 11(1):11579, 2021. (Cited on page 14.)

K. Kim, Y. Oh, and J. C. Ye. Zegot: Zero-shot segmentation through optimal transport of text prompts. *arXiv preprint arXiv:2301.12171*, 2023. (Cited on page 8.)

T. N. Kipf and M. Welling. Semi-supervised classification with graph convolutional networks. *International Conference on Learning Representations*, 2017. (Cited on page 17.)

B. Li, Y. Li, and K. W. Eliceiri. Dual-stream multiple instance learning network for whole slide image classification with self-supervised contrastive learning. In *Proceedings of the IEEE/CVF conference on computer vision and pattern recognition*, pages 14318–14328, 2021. (Cited on pages 4, 11, 12, and 13.)

H. Li, C. Zhu, Y. Zhang, Y. Sun, Z. Shui, W. Kuang, S. Zheng, and L. Yang. Task-specific fine-tuning via variational information bottleneck for weakly-supervised pathology whole slide image classification. In *Proceedings of the IEEE/CVF Conference on Computer Vision and Pattern Recognition*, pages 7454–7463, 2023. (Cited on page 2.)

X. L. Li and P. Liang. Prefix-tuning: Optimizing continuous prompts for generation. *Proceedings of the 59th Annual Meeting of the Association for Computational Linguistics and the 11th International Joint Conference on Natural Language Processing (Volume 1: Long Papers)*, 2021. (Cited on pages 2 and 3.)

Z. Li, L. Zhao, Z. Zhang, H. Zhang, D. Liu, T. Liu, and D. N. Metaxas. Steering prototypes with prompt-tuning for rehearsal-free continual learning. In *Proceedings of the IEEE/CVF Winter Conference on Applications of Computer Vision*, pages 2523–2533, 2024. (Cited on page 5.)

M. Liero, A. Mielke, and G. Savaré. Optimal entropy-transport problems and a new hellinger–kantorovich distance between positive measures. *Inventiones mathematicae*, 211(3):969–1117, 2018. (Cited on page 18.)

T. Lin, Z. Yu, H. Hu, Y. Xu, and C.-W. Chen. Interventional bag multi-instance learning on whole-slide pathological images. In *Proceedings of the IEEE/CVF Conference on Computer Vision and Pattern Recognition*, pages 19830–19839, 2023. (Cited on pages 2, 12, and 13.)

M. Y. Lu, D. F. Williamson, T. Y. Chen, R. J. Chen, M. Barbieri, and F. Mahmood. Data-efficient and weakly supervised computational pathology on whole-slide images. *Nature biomedical engineering*, 5(6):555–570, 2021. (Cited on pages 4, 7, 11, 12, and 13.)

M. Y. Lu, B. Chen, A. Zhang, D. F. Williamson, R. J. Chen, T. Ding, L. P. Le, Y.-S. Chuang, and F. Mahmood. Visual language pretrained multiple instance zero-shot transfer for histopathology images. In *Proceedings of the IEEE/CVF conference on computer vision and pattern recognition*, pages 19764–19775, 2023. (Cited on pages 2 and 4.)

M. Y. Lu, B. Chen, D. F. Williamson, R. J. Chen, I. Liang, T. Ding, G. Jaume, I. Odintsov, L. P. Le, G. Gerber, et al. A visual-language foundation model for computational pathology. *Nature Medicine*, 30(3):863–874, 2024. (Cited on pages 4, 11, 12, 13, 14, and 16.)

Y. Lu, J. Liu, Y. Zhang, Y. Liu, and X. Tian. Prompt distribution learning. In *Proceedings of the IEEE/CVF Conference on Computer Vision and Pattern Recognition*, pages 5206–5215, 2022. (Cited on page 5.)

A. Madabhushi and G. Lee. Image analysis and machine learning in digital pathology: Challenges and opportunities. *Medical image analysis*, 33:170–175, 2016. (Cited on page 2.)

D. Nechaev, A. Pchelnikov, and E. Ivanova. Hibou: A family of foundational vision transformers for pathology. *arXiv preprint arXiv:2406.05074*, 2024. (Cited on page 4.)

D. M. Nguyen, N. T. Diep, T. Q. Nguyen, H.-B. Le, T. Nguyen, T. Nguyen, T. Nguyen, N. Ho, P. Xie, R. Wattenhofer, et al. Logra-med: Long context multi-graph alignment for medical vision-language model. *arXiv preprint arXiv:2410.02615*, 2024a. (Cited on page 8.)

D. M. Nguyen, A. T. Le, T. Q. Nguyen, N. T. Diep, T. Nguyen, D. Duong-Tran, J. Peters, L. Shen, M. Niepert, and D. Sonntag. Dude: Dual distribution-aware context prompt learning for large vision-language model. *Asian Conference on Machine Learning (ACML)*), 2024b. (Cited on page 3.)

H. Nguyen, K. Le, Q. Nguyen, T. Pham, H. Bui, and N. Ho. On robust optimal transport: Computational complexity and barycenter computation. In *Advances in NeurIPS*, 2021. (Cited on page 3.)

M. K. K. Niazi, A. V. Parwani, and M. N. Gurcan. Digital pathology and artificial intelligence. *The lancet oncology*, 20(5):e253–e261, 2019. (Cited on page 1.)

A. v. d. Oord, Y. Li, and O. Vinyals. Representation learning with contrastive predictive coding. *arXiv preprint arXiv:1807.03748*, 2018. (Cited on page 6.)

L. Pantanowitz, P. N. Valenstein, A. J. Evans, K. J. Kaplan, J. D. Pfeifer, D. C. Wilbur, L. C. Collins, and T. J. Colgan. Review of the current state of whole slide imaging in pathology. *Journal of pathology informatics*, 2(1):36, 2011. (Cited on page 1.)

G. Peyré, M. Cuturi, et al. Computational optimal transport: With applications to data science. *Foundations and Trends® in Machine Learning*, 11(5-6):355–607, 2019. (Cited on page 17.)

K. Pham, K. Le, N. Ho, T. Pham, and H. Bui. On unbalanced optimal transport: An analysis of Sinkhorn algorithm. In *International Conference on Machine Learning*, pages 7673–7682. PMLR, 2020. (Cited on pages 3 and 19.)

L. Qu, K. Fu, M. Wang, Z. Song, et al. The rise of ai language pathologists: Exploring two-level prompt learning for few-shot weakly-supervised whole slide image classification. *Advances in Neural Information Processing Systems*, 36, 2024a. (Cited on pages 3, 5, 8, 11, and 12.)

L. Qu, D. Yang, D. Huang, Q. Guo, R. Luo, S. Zhang, and X. Wang. Pathology-knowledge enhanced multi-instance prompt learning for few-shot whole slide image classification. *arXiv preprint arXiv:2407.10814*, 2024b. (Cited on page 2.)

A. Radford, J. W. Kim, C. Hallacy, A. Ramesh, G. Goh, S. Agarwal, G. Sastry, A. Askell, P. Mishkin, J. Clark, et al. Learning transferable visual models from natural language supervision. In *International conference on machine learning*, pages 8748–8763. PMLR, 2021. (Cited on page 3.)

Y. Rao, W. Zhao, G. Chen, Y. Tang, Z. Zhu, G. Huang, J. Zhou, and J. Lu. Denseclip: Language-guided dense prediction with context-aware prompting. In *Proceedings of the IEEE/CVF conference on computer vision and pattern recognition*, pages 18082–18091, 2022. (Cited on page 5.)

J. Ryu, A. V. Puche, J. Shin, S. Park, B. Brattoli, J. Lee, W. Jung, S. I. Cho, K. Paeng, C.-Y. Ock, et al. Ocelot: overlapped cell on tissue dataset for histopathology. In *Proceedings of the IEEE/CVF Conference on Computer Vision and Pattern Recognition*, pages 23902–23912, 2023. (Cited on page 2.)

T. Séjourné, G. Peyré, and F.-X. Vialard. Unbalanced optimal transport, from theory to numerics. *Handbook of Numerical Analysis*, 24:407–471, 2023. (Cited on pages 3 and 8.)

Z. Shao, H. Bian, Y. Chen, Y. Wang, J. Zhang, X. Ji, et al. Transmil: Transformer-based correlated multiple instances learning for whole slide image classification. *Advances in neural information processing systems*, 34:2136–2147, 2021. (Cited on pages 4, 11, 12, and 13.)

J. Shi, L. Tang, Y. Li, X. Zhang, Z. Gao, Y. Zheng, C. Wang, T. Gong, and C. Li. A structure-aware hierarchical graph-based multiple instance learning framework for pt staging in histopathological image. *IEEE Transactions on Medical Imaging*, 42(10):3000–3011, 2023. (Cited on page 2.)

J. Shi, C. Li, T. Gong, Y. Zheng, and H. Fu. Vila-mil: Dual-scale vision-language multiple instance learning for whole slide image classification. In *Proceedings of the IEEE/CVF Conference on Computer Vision and Pattern Recognition*, pages 11248–11258, 2024. (Cited on pages 2, 3, 4, 5, 6, 7, 10, 11, 12, 13, and 16.)

M. Shu, W. Nie, D.-A. Huang, Z. Yu, T. Goldstein, A. Anandkumar, and C. Xiao. Test-time prompt tuning for zero-shot generalization in vision-language models. *Advances in Neural Information Processing Systems*, 35:14274–14289, 2022. (Cited on page 5.)

S. P. Singh and M. Jaggi. Model fusion via optimal transport. *Advances in Neural Information Processing Systems*, 33:22045–22055, 2020. (Cited on page 8.)

A. H. Song, G. Jaume, D. F. Williamson, M. Y. Lu, A. Vaidya, T. R. Miller, and F. Mahmood. Artificial intelligence for digital and computational pathology. *Nature Reviews Bioengineering*, 1(12):930–949, 2023. (Cited on page 2.)

W. Tang, S. Huang, X. Zhang, F. Zhou, Y. Zhang, and B. Liu. Multiple instance learning framework with masked hard instance mining for whole slide image classification. In *Proceedings of the IEEE/CVF International Conference on Computer Vision*, pages 4078–4087, 2023. (Cited on page 2.)

W. Tang, F. Zhou, S. Huang, X. Zhu, Y. Zhang, and B. Liu. Feature re-embedding: Towards foundation model-level performance in computational pathology. In *Proceedings of the IEEE/CVF Conference on Computer Vision and Pattern Recognition*, pages 11343–11352, 2024. (Cited on pages 11 and 12.)

The Cancer Genome Atlas (TCGA). Genomic Data Commons Data Portal (GDC). <https://portal.gdc.cancer.gov/projects/TCGA-BRCA>. Accessed 07 Jul. 2023. (Cited on pages 10 and 16.)

M. Tsuneki and F. Kanavati. Inference of captions from histopathological patches. In *International Conference on Medical Imaging with Deep Learning*, pages 1235–1250. PMLR, 2022. (Cited on pages 3 and 10.)

A. Vaswani. Attention is all you need. *Advances in Neural Information Processing Systems*, 2017. (Cited on pages 2 and 7.)

P. Veličković, G. Cucurull, A. Casanova, A. Romero, P. Lio, and Y. Bengio. Graph attention networks. *arXiv preprint arXiv:1710.10903*, 2017. (Cited on page 8.)

C. Villani et al. *Optimal transport: old and new*, volume 338. Springer, 2009. (Cited on page 17.)

G. Xu, Z. Song, Z. Sun, C. Ku, Z. Yang, C. Liu, S. Wang, J. Ma, and W. Xu. Camel: A weakly supervised learning framework for histopathology image segmentation. In *Proceedings of the*

IEEE/CVF International Conference on computer vision, pages 10682–10691, 2019a. (Cited on page 2.)

H. Xu, N. Usuyama, J. Bagga, S. Zhang, R. Rao, T. Naumann, C. Wong, Z. Gero, J. González, Y. Gu, et al. A whole-slide foundation model for digital pathology from real-world data. *Nature*, pages 1–8, 2024. (Cited on pages 2, 3, 4, and 12.)

K. Xu, W. Hu, J. Leskovec, and S. Jegelka. How powerful are graph neural networks? *International Conference on Learning Representations*, 2019b. (Cited on page 17.)

H. Yao, R. Zhang, and C. Xu. Tcp: Textual-based class-aware prompt tuning for visual-language model. In *Proceedings of the IEEE/CVF Conference on Computer Vision and Pattern Recognition*, pages 23438–23448, 2024. (Cited on pages 2, 3, and 5.)

F. Zhan, Y. Yu, K. Cui, G. Zhang, S. Lu, J. Pan, C. Zhang, F. Ma, X. Xie, and C. Miao. Unbalanced feature transport for exemplar-based image translation. In *Proceedings of the IEEE/CVF conference on computer vision and pattern recognition*, pages 15028–15038, 2021. (Cited on page 3.)

H. Zhang, Y. Meng, Y. Zhao, Y. Qiao, X. Yang, S. E. Coupland, and Y. Zheng. Dtfd-mil: Double-tier feature distillation multiple instance learning for histopathology whole slide image classification. In *Proceedings of the IEEE/CVF conference on computer vision and pattern recognition*, pages 18802–18812, 2022a. (Cited on pages 12 and 13.)

Y. Zhang, H. Fei, D. Li, T. Yu, and P. Li. Prompting through prototype: A prototype-based prompt learning on pretrained vision-language models. *arXiv preprint arXiv:2210.10841*, 2022b. (Cited on page 5.)

C. Zhao, Y. Wang, X. Jiang, Y. Shen, K. Song, D. Li, and D. Miao. Learning domain invariant prompt for vision-language models. *IEEE Transactions on Image Processing*, 2024. (Cited on pages 8, 11, and 12.)

Y. Zheng, R. H. Gindra, E. J. Green, E. J. Burks, M. Betke, J. E. Beane, and V. B. Kolachalama. A graph-transformer for whole slide image classification. *IEEE transactions on medical imaging*, 41(11):3003–3015, 2022. (Cited on pages 4, 12, and 13.)

K. Zhou, J. Yang, C. C. Loy, and Z. Liu. Conditional prompt learning for vision-language models. In *Proceedings of the IEEE/CVF conference on computer vision and pattern recognition*, pages 16816–16825, 2022a. (Cited on pages 5, 8, 11, and 12.)

K. Zhou, J. Yang, C. C. Loy, and Z. Liu. Learning to prompt for vision-language models. *International Journal of Computer Vision*, 130(9):2337–2348, 2022b. (Cited on pages 2, 3, 5, 8, 11, and 12.)